2017 Update on the WFC3/UVIS Stability and Contamination Monitor

C. E. Shanahan, C. M. Gosmeyer, S. Baggett

June 9, 2017

ABSTRACT

The photometric throughput of the UVIS detector on WFC3 is monitored each cycle for its stability as a function of time, wavelength, as well as to check for any evidence of contamination on the CCD windows, which would manifest as a decrease in throughput strongest in the bluest filters. This program has been in place since the installation of WFC3 in 2009, historically making periodic observations of the spectrophotometric standard GRW+70d5824 (GRW70) in several key filters from 200 nm to 600 nm, with red filters acting as a control. This is a follow up report to the last analysis of the temporal stability of UVIS (Gosmeyer et al., 2014), since which several major changes to the program and data analysis have been implemented. Due to recent work suggesting a low-level, long-term variability for GRW70, another spectrophotometric standard star - GD153 - has been added to the program and is now analyzed in conjunction with GRW70. Data are now processed with the latest version of the CALWF3 calibration pipeline (v. 3.4), which has several new features that represent a paradigm shift in calibration methodology. Finally, the data analysis software, which was previously entirely IRAF based, was re-written in Python. We find a steady decline in the count rate for most filters but no evidence for contamination, which would manifest as a wavelength-dependent effect, impacting bluer filters more strongly. These declines range from 0.01% to 0.3% per year, and are stronger in longer wavelength filters. Similar temporal changes are found for both stars, and the long-term trends in throughput agree with previous trends derived in 2014.

1. Introduction

Temporal and optical stability are a defining advantage of the Hubble Space Telescope (HST) over ground-based instruments. To ensure the optimum calibration for all on-orbit observations, it is necessary to monitor the instruments for long-term trends in both spatial and temporal stability. Programs that monitor the spatial stability of the detectors, for example, can look for variations in flat fields by measuring the countrates for the same star on different locations on the detector. Making periodic observations of high signal-to-noise, bright, isolated stars, and looking for long-term trends in measured flux can assess temporal stability. We report on the photometric throughput stability as a function of time and wavelength for the UVIS channel on Wide Field Camera 3 (WFC3). This study also allows us to determine if contamination is present on the CCD windows by looking for a stronger decline in the measured photometry in short wavelength filters.

Such a program has been in place since the Servicing Mission Observatory Verification (SMOV) period after the installation of the camera in 2009, for both the IR and the UVIS channels. The UVIS channel, the focus of this report, covers the 200-1000nm spectral range and consists of two 2K4K CCD chips, 62 filters, and one grism. Due to differences in the two chips properties and behaviors, especially at UV wavelengths, we monitor the two chips independently in our characterization of detector stability. In this most recent analysis, we make use of the latest chip-dependent photometric calibration for the UVIS detector which was delivered in February 2016. Historically, the UVIS contamination monitor has involved imaging the spectrophotometric standard white dwarf star GRW+70D5824 in a key set of UVIS and IR filters, as well as the UVIS grism. In this work, we extend the calibration program to include a second spectrophotometric standard white dwarf star GD153, in case of potential variability in GRW70.
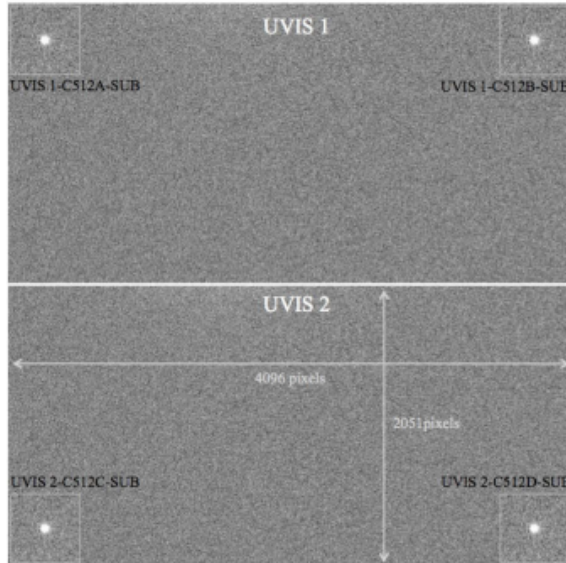
Fig. 1.— Locations of the four corner 512 pixel subarrays, to scale. We minimize the readout overheads and maximize the number of exposures per orbit by imaging in these subarrays rather than in the full two chips. Additionally, effects of CTE are minimal when imaging is done close to the readout amplifiers. Figure from Kalirai et al. (2010).

This report is an update to Gosmeyer et al. 2014 (G14). Since their report, we have made several major changes to the observing program and data analysis. These key changes are summarized below, with a more thorough discussion in subsequent sections:

- In addition to GRW70, another white dwarf standard GD153 is now included in the temporal stability characterization. This choice is in response to recent analysis suggesting a low level, long-term variability of GRW70.

- All observations are now calibrated with the most recent version of the IRAF/STSDAS pipeline program CALWF3 version 3.4, with a common set of reference files. This updated calibration pipeline has several major updates for calibration of UVIS images. These include a chip-dependent solution for photometric calibration, improved reference files (darks and flat fields), and the ability to correct for flux losses due to the declining charge transfer efficiency (CTE). The latest version also includes updated inverse sensitivity values in the UVIS photometry lookup table (IMPHTTAB), which CALWF3 uses to populate photometry header keywords and to scale the UVIS2 science array by the chip inverse sensitivity ratio, such that photometry is continuous across the full UVIS detector.

- The data analysis pipeline for observations has been rewritten entirely in Python. IRAF tasks were used previously to remove cosmic rays from calibrated images, perform source finding and aperture photometry, and for all statistical calculations on the data and in the derivation of long term trends and errors.

1. Data

Currently, two spectrophotometric standard white dwarf stars are observed for the UVIS temporal stability and contamination monitor. The spectra and characteristics of these stars, GRW+70D5824 (GRW70) and GD153, are detailed in Table 1.
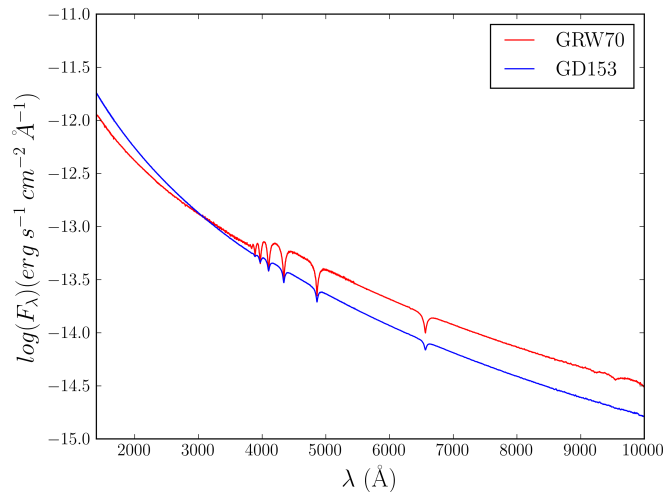
	RA (2000)	Dec (2000)	V mag	B-V	Spectral Type
GRW70	13h 38m 51.77s	+70d 17' 08.5"	12.77	-0.09	DA3
GD153	12h 57m 02.37s	+22d 01' 56.0"	13.35	-0.29	DA1

Table 1: Spectra and characteristics of our white dwarf spectroscopic standards, GRW+70D5824 and GD153. From the HST CALSPEC Calibration Database (http://www.stsci.edu/hst/observatory/crds/calspec.html).

GRW70 is part of the original set of standard stars chosen for HST (Bohlin, 1996) and has been observed periodically since the installation of WFC3 in 2009. This star has also been used as a monitor for other HST instruments including STIS (Stys et al., 2001), WFPC2 (Whitmore et al., 1996), and ACS (DeMarchi et al., 2004, Sirianni et al., 2005).

Initially, observations of GRW70 were taken once a week for the UVIS contamination and stability monitor. Due to the excellent performance of the instrument, observations have been decreased to the present frequency of about once every five weeks starting in late-2010 (Cycle 18) and continuing through late-2015 (Cycle 22).

Recent analysis of ground-based observation of GRW70 suggests that the star's flux may exhibit a low-level, long-term variability. The star exhibited a decrease in throughput of 5-6 mmag/yr in U and B (3 sigma significance) and a decrease in VRI of 3 mmag/yr (2 sigma significance) (Bohlin, R., Landolt, A., 2015). Due to the questionable stability of GRW70, in cycle 23 we began the transition to another white dwarf spectrophotometric standard (GD153), which is now monitored every five weeks. We leave a small number of contemporaneous GRW70 visits (once every three months) to tie results from the new standard back to past monitor data. Data from the photometric and zero point monitors for UVIS provide images of GD153 from SMOV to the present in several filters, allowing for long-term trends to be analyzed.

A summary of all imaging data is provided in Table 2 and Table 3 for GRW70 and GD153, respectively. Our data primary come from the dedicated contamination and stability monitoring programs, but as mentioned we also incorporate data from photometry and zeropoint monitoring programs to extend the coverage of GD153 back to cycle 18.

A majority of observations are taken in the UVIS1-C512A-SUB (Quadrant A) and UVIS1-C512C-SUB (Quadrant C) corner subarrays, 512 x 512 pixel subarrays located on the corners of the WFC3 4k4k mosaic near the A and C read out amplifiers, respectively (see Figure 1). Due to the incorporation of photometric calibration programs (HST programs 12699, 12334, and 13575) to extend coverage of GD153 to cycle 18, we include images taken in the middle 512 pixel subarray UVIS2-M512C-SUB in our analysis. Only images taken in these three subarrays are included in the final calculations of throughput trends with time in each filter. We have a small number of images taken in the corner subarrays near amps B and D (UVIS1-C512B-SUB and UVIS2-C512D-SUB), but these are not included in calculations of throughput trends.

We use corner subarrays close to the amplifiers in order to minimize readout overhead and buffer dumps. This allows us to pack in the maximum number of exposures in each orbit. The use of corner subarrays also helps to mitigate the effects of charge transfer efficiency (CTE) decline due to on-orbit radiation damage. For this reason, as well as the use of post-flash starting in Cycle 20 (Feb 2013) and the large aperture size used for photometry, we do not correct the subarray data for CTE losses.

Early in the mission, exposure times were kept low (proposals CAL11426 and CAL11907)

in order to avoid any possibility of saturation. Exposure times have since been increased where possible to improve signal-to-noise.

All data after Cycle 20 is post-flashed to to elevate the background level and to mitigate CTE losses. CTE losses are greatest for faint targets and images with low background levels (Noeske et al., 2012). In our data, background levels are low due to the relatively short exposure times. However, CTE effects are negligible still due to the brightness of the stars, imaging in corner subarrays close to the readout amplifier, and the large 10 pixel (0.4 arcsec) aperture used for aperture photometry. Nevertheless, starting in Cycle 20 we began post-flashing all data for consistency if any CTE effects become evident in the future as the detector ages, despite our precautions. G14 performed a crosscheck of flashed data to non-flashed data and found that fluxes and background levels agreed to 1%, with no indication of a jump due to the post-flash.

2.1 Critical Filters

As shown in Table 2 and Table 3, images of the standard stars are actively obtained in a subset 19 UVIS filters. The filters cover the Narrow (N), Medium (M), Wide (W), and Long Pass (LP) bands. When zeropoint and photometry data are included, we have data for all 62 UVIS filters + 1 grism. Of the filters we obtain images in, we focus our analysis on what we define as a critical subset of seven UVIS filters. These filters include five blue filters; F218W, F225W, F275W, F336W, and F438W. In addition, we include longer wavelength filters F606W and F814W as controls to compare to the throughput trends in the UV. An offset in throughput stability between UV and control filters is a sign of contamination. This critical set of filters, which were chosen to best assess for contamination effects, have the greatest number of observations and have had continuous coverage from SMOV to the present. The purpose of continuing to collect data in all filters is a safeguard in the event that we do detect contamination in the critical set of filters.

3. Analysis

To analyze the temporal photometric stability of the UVIS detector and monitor for contaminants on the CCD windows, we measure the countrate of standard stars GRW70 and GD153 over time in several short wavelength UVIS filters, with a set of redder filters acting as a control. Raw images are processed with version 3.4 of the WFC3 calibration pipeline CALWF3. We then remove cosmic rays with the Python implementation of the Laplacian

edge detection program LAcosmic (van Dokkum, 2001), correct for geometric distortion by applying a pixel area map (PAM), create a source list with photutils/DAOstarfinder, calculate and subtract background levels using an iterative sigma clipping routine, and finally perform point source photometry with a 10 pixel aperture radius, using photutils/aperture_photometry. Countrates are calculated by taking the sky-subtracted fluxes (in e-) within the 10 pixel aperture radius and dividing by the exposure time. With countrates measured for each observation, we define the parameter Δ Flux as the percent change in countrate over time, with respect to a baseline value defined as the median of all observations taken on the first visit.

The following section will discuss in further detail how we derive countrates (e-/s) from the science images. Additionally, we will discuss the key differences in the photometry analysis from G14s study of the temporal stability of UVIS.

3.1 New WFC3 calibration pipeline

Calibrated files are retrieved and analyzed as they are delivered to the archive. Currently in Cycle 24, new data is obtained every 5 weeks for GD153 and once every 3 months for GRW70. Calibrated images (FLTs) are retrieved from the Mikulski Archive for Space Telescopes (MAST). It is possible to calibrate raw images on the fly with a standalone version of the calibration pipeline, but we choose to retrieve from MAST, the simplest way to assert that all observations are processed with a common set of the most up to date reference files and software.

All observations from SMOV onward are processed with a common set of reference files using the IRAF/STSDAS pipeline program CALWF3 (version 3.4) in the wfc3tools package, available as part of stsci_python. This same pipeline is used to calibrate observations for general observers. CALWF3 applies bias, post-flash, and dark image subtraction, flat-fielding and gain conversion to produce calibrated data in units of electrons. CALWF3 version 3.4 is the most recent version of the WFC3 calibration pipeline with several major updates (Ryan et al., 2016). The use of the version 3.4 pipeline to calibrate the raw data is one of the major updates since the 2014 report.

Several new features originally introduced to CALWF3 with the release of version 3.3 in February 2016 represent a paradigm shift in calibration methodology. Most notably, the two UVIS chips are now treated as independent detectors in the pipeline with separate photometric calibrations. UVIS1 and UVIS2 exhibit very different quantum efficiencies, especially in the UV at $\lambda < 3500$ Å, where UVIS2 is more sensitive than UVIS1. For

this reason, the updated pipeline implements a chip dependent photometric calibration. A new header key word PHTRATIO (PHTFLAM2/PHTFLAM1, the inverse sensitivity ratio between chips) allows CALWF3 to scale UVIS2 to match UVIS1 to ensure sources have the same countrate on each chip. Additionally, though we are making relative measurements of countrates on each chip, it is important to note that independently calculated zeropoints for each chip ensure flux is continuous across UVIS1 and UVIS2 as well (Deustua et al., 2016).

The updated calibration pipeline (CALWF3 v. 3.3 and later) also includes improved reference files. The chip dependent calibration approach means that the UVIS flat fields were recomputed and normalized to the median value of each chip separately, removing sensitivity offsets from the flats (Mack et al., 2016). Additionally, updated flats for the four bluest UV filters have corrected for spatial crosshatching pattern on the flats that responsible for sensitivity residuals at the level of a few percent (Mack, 2016).

See Ryan et al. 2016 for more information about other features updated pipeline, including the incorporation of a CTE correction switch for full frame images. Note that the CTE correction for subarrays was released in CALWF3 v3.4, but we do not make use of these features for reasons discussed in Section 2.

3.2 Sky subtraction and geometric distortion correction

Sky levels are calculated and subtracted for each FLT, before the pixel area map is applied. We define sky pixels as all pixels excluding a 80 pixel circular radius from the center of the source and a 10 pixel border around the subarray. We use an iterative sigma clipping routine to clip out anomalous pixels (unflagged hot pixels, for example), and define the sky level as the median of the distribution of clipped pixels in this region.

We correct the FLTs for geometric distortion using the pixel area map (available at http://www.stsci.edu/hst/wfc3/pam/pixel_area_maps) for each subarray.

3.3 Cosmic Ray Rejection

Next, calibrated images that have been corrected for geometric distortion are cleaned of cosmic rays with the Laplacian edge detection program LAcosmic. This algorithm takes a small set of user-defined parameters and identifies and masks cosmic rays of arbitrary shapes and sizes by the sharpness of their edges (van Dokkum, 2001). This algorithm is iterative, and cosmic rays are replaced by the median of surrounding unaffected pixels. LAcosmic is robust at removing cosmic rays from images, and allows a greater sample size to be obtained

by not drizzling together dithered exposures to correct cosmic rays. The source countrate for images cleaned by drizzling and images cleaned by IRAF/LACOSMIC agree to a small fraction of a percent (Kalirai et al. 2010).

G14 used the IRAF version of LACOSMIC. Now, we use the same algorithm but implemented in Python (cosmics.py by Malte Tewes). Detection thresholds and parameters were set individually for each filter by iterating over several combinations of parameters and generating diagnostic output that allowed for the best set of parameters to be chosen. We carry out visual inspection of each image to check for erroneous cosmic ray flags in the source star. Over-flagged images account for less than 1% of our total dataset, and since we have many thousands of images, we have not attempted to salvage the discarded images by setting detection thresholds manually for this small set of observations. G14 found approximately 5% of observations were over-flagged by IRAF/LACOSMIC, so our 1% fraction of discarded data is a good improvement.

When comparing post-flashed and non post-flashed images, LACOSMIC tends to flag more pixels than necessary in the background of the post-flashed images, and this can lower the measured background value slightly (G14). However, the effect of the lower background on the final star flux is negligible since the total number of counts from within the aperture is large (>300,000 electrons).

3.3 Point Source Photometry

We perform aperture photometry on calibrated, PAM corrected, and cosmic ray masked images, where masked pixels are interpolated with surrounding 'good' pixels. In G14s analysis, source finding and aperture photometry were done with IRAF/DAOFIND and IRAF/DAOPHOT, respectively. We now use similar tasks within the Python Photutils package. A recent comparison between photometry software found that at a 0.4 arcsecond aperture radius, the aperture sums produced by IRAF/DAOFIND and Photutils aperture photometry are only discrepant by 0.1% at small aperture radii (r=3 pixels) and agree to within 0.01% at 10 pixels (Bajaj, Khandrika, 2017).

Source lists are generated with Photutils.DAO_star_finder. We use a 10 pixel (0.4 arc second) circular aperture radius and Photutils.aperture_photometry to measure fluxes. By setting appropriate detection thresholds for each filter, flagging cosmic rays, and removing the handful of images where the source star was masked as a cosmic ray, we do not encounter issues with source finding resulting in no or multiples sources.

Currently, photutils.aperture_photometry does not yet compute photometric errors for

each measurement. We calculate these errors in the same manner as DAOPHOT -

$$error = sqrt(flux/epadu + area * stdev^2 + area^2 * stdev^2/nsky)$$

- where epdadu is the nominal gain in the detector quadrant (e- / ADU) , nsky is the sky level and stdev is the sky RMS.

For each image, countrate (in electrons per second) is found by dividing the flux in the aperture (in electrons) by the exposure time.

3.4 Percent change in flux

We define a parameter Δ Flux (%) to analyze trends in throughput over time from countrates measured in observations spanning from SMOV to the present. This value is the percent change in flux, defined with respect to a baseline countrate value for each filter and CCD chip for both GRW70 and GD153. The baseline countrate value we choose is the median of all observations taken within 50 days of the first observation in that particular subset of the data. A 50-day window was chosen to ensure that all observations from the first few sets of observations are included in the calculation of this initial countrate.

By measuring the slope of Δ Flux (%) over time, we can assess the temporal stability, and look for signs of contamination in the blue filters. We can also use this to compare any drifts in sensitivity between UVIS1 and UVIS2 or to look for any offsets in the count rate between chips.

3.5 Measuring throughput stability

To assess any temporal changes, we perform a linear fit to Δ flux and time (Modified Julian Date, or MJD), and also compute the standard deviation of all measurements for each filter and chip using the polyfit function the Python numpy library. These fits are weighted by errors in Δ Flux, calculated using standard error propagation from the individual errors in countrate for each image. In the previous analysis, this was done with IRAF/ tlinear. In a comparison between the output of IRAF/tlinear and polyfit, we did not see any differences between the two fitting functions. We used both polyfit and IRAF/tlinear on data processed with the G14 analysis pipeline, using images that were processed with the older version of CALWF3, and found the resulting slopes agreed to floating point precision. The linear fits to the data are weighted by the measurement errors, which are slightly larger in the earliest measurements where exposure times were more conservative.

We use Monte Carlo simulations to constrain the individual linear fits. In these simulations, we select a random subset of the data for each filter and chip combination and calculate the parameters of the best linear fit with numpy.polyfit. These subsets are half of the dataset, randomly chosen for 10000 iterations. The distributions of calculated slopes for these 100000 random subsets are very closely Gaussian (Figure 2).
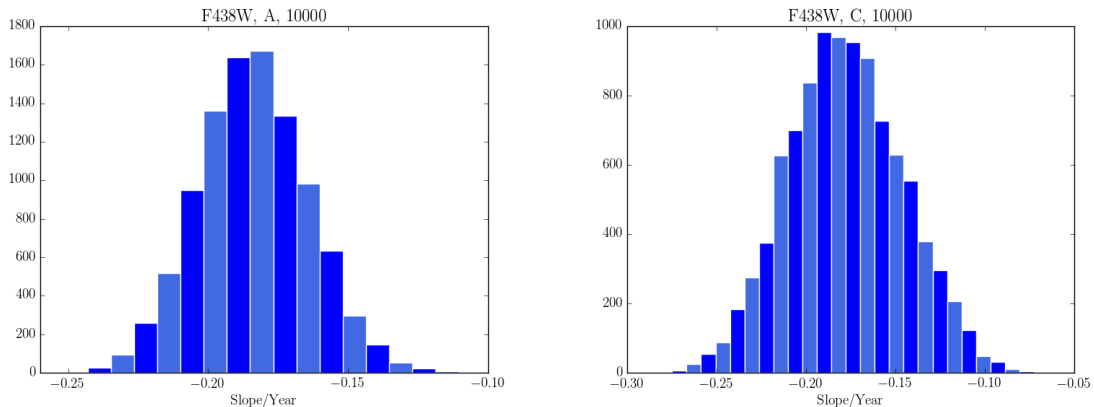

Fig. 2.— Results for filter F438W, amplifiers A (left) and C (right) of 10,000 Monte Carlo simulations performed on the slope of Δ flux (%) versus time. The distributions are approximately Gaussian

4. Results and Discussion

Measuring the change in observed countrate of flux-stable stars on the UVIS detector provides a means of assessing the stability of photometric throughput over time. This procedure also allows throughput stability as a function of wavelength to be assessed by comparing observations in several filters. Finally, we are able to use these results to check for the presence of contaminants on the CCD windows by looking for an offset between throughput declines in the UV and in the longer wavelength control filters.

We focus our analysis on the critical set of blue filters and the red control filters. We do have significant coverage over time of GRW70 in an additional set of 5 filters (F390M, F467M, F547M, F555W, and F850LP), so results from these filters are included for completeness in Figure 9 and Table 4 but are not addressed in the discussion.

Figures 8 and Figure 10 show Δ flux for each observation over time for the critical set of seven UVIS filters for GRW70 and GD153, respectively. These observations are split between UVIS1 and UVIS2 (in the top and bottom panels, respectively), and the linear fit

11

is only applied to data in the UVIS2-C512A-SUB (Quadrant A) and UVIS2-C512C-SUB (Quadrant C) subarrays. Figure 9 shows the results for the additional wavelength coverage we obtained for GRW70.

Table 4 and Table 5 summarize the long-term trends in throughput in each filter / chip for GRW70 and GD153, respectively. In these tables, slopes are reported in Δ Flux per year, the Mean and Stdev columns are the mean slope and standard deviations from the distribution of random slopes from the Monte Carlo simulations, respectively.

4.1 Scatter in results

In the 2014 report, photometry from early in the mission (prior to 31 Oct 2010, MJD=55500) showed a large scatter in the UV filters F218W, F225W and F275W. With the reprocessed and reanalyzed data, we no longer see a large scatter in countrate from early observations in the three bluest UV filters. We attribute the decrease in scatter to the improved UV flatfield reference files delivered in 2016. These flats correct for spatial residuals in sensitivity due to the lower in-flight temperature, -82° C versus -49° C for the UV flats obtained from ground test data (Mack, 2016).

The UV flatfields exhibited prominent 'crosshatching' structures (Mack et al., 2013), strongest in the bluest filters (2-3%), and most pronounced on UVIS1. If the stars position on the chip varies from visit to visit, it falls on and off these structures and the measured flux will vary based on position. As seen in Figure 3, the location of GRW70 on the subarray varied significantly visit to visit in the earliest observations, forming an annulus around the center of the detector where the pointing was supposed to be centered. This suggests a proper motion residual introduced in the observing proposal, the ring shape resulting from the varying orientation of each visit throughout the year. Since (31 Oct 2010, MJD=55500), a more accurate proper motion has been updated in the proposal and the star is well centered on the subarrays, and this is why the large scatter was not seen in later observations by G14.
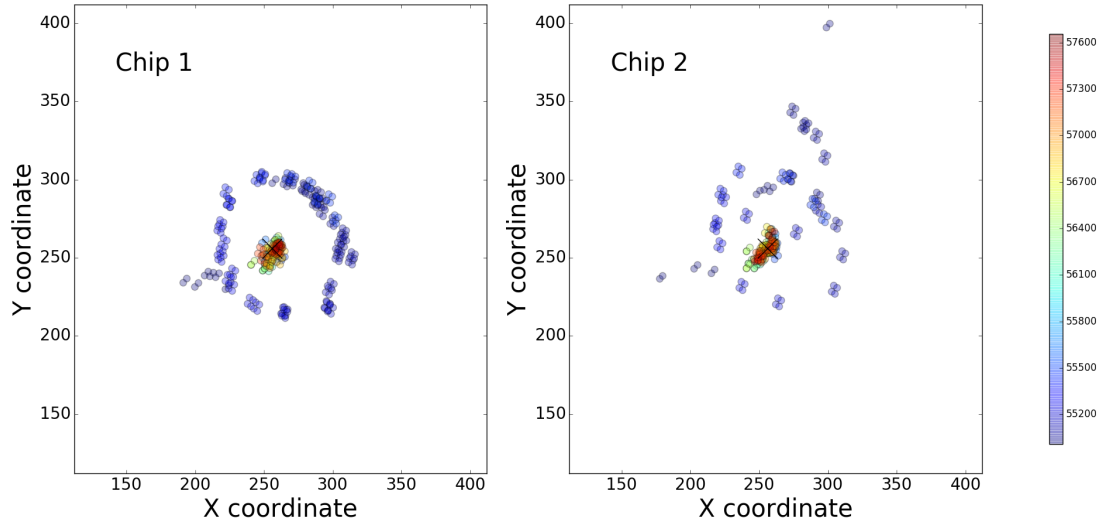
Fig. 3.— Position of GRW70 on the Quadrant A and Quadrant C corner 512x512 pixel subarrays, color coded by date. Inaccurate proper motion of the source in these early visits resulted in the position of the star on the chip moving considerably from visit to visit. Later proposals corresponding to dates MJD>55500 include updated values of the proper motion, which improved the centering of the source in the subarray.

There was more scatter in countrate on UVIS than on UVIS2, consistent with the difference in crosshatch strength between the two chips. Figure 4 shows the standard deviation in Δ Flux vs. time for the full data set on UVIS1, on data processed with both the 2014 flatfields and the improved 2016 flatfields. The scatter in the UV filters has been brought down to the level of the longer wavelength filters after processing data with the 2016 flat fields.
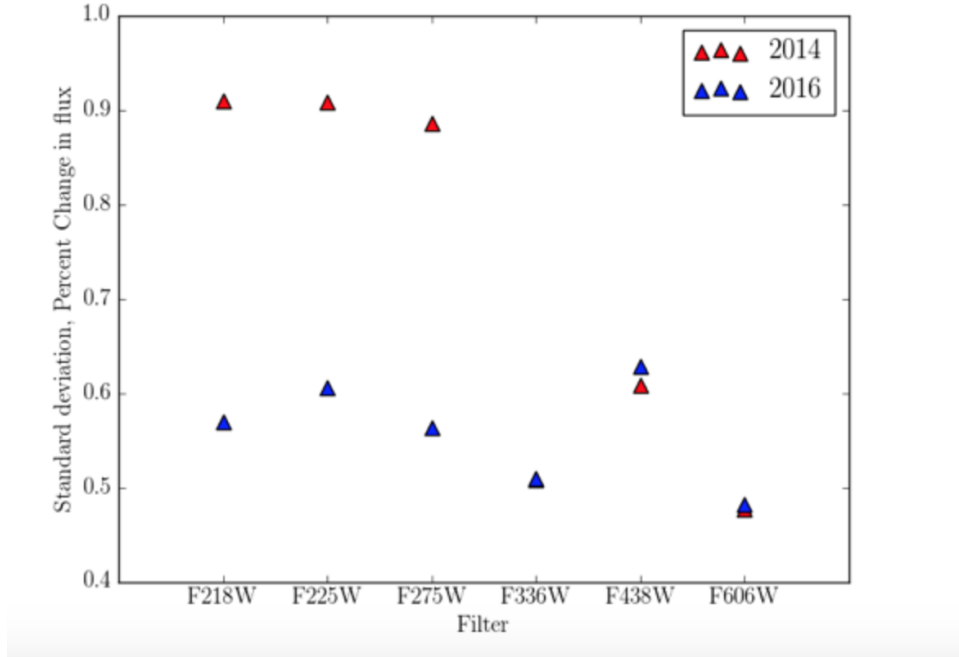
Fig. 4.— For each filter in the critical set, the standard deviation in the earliest observations (before 31 Oct. 2010, MJD<55500) for data processed with the old flatfields (red) and the improved UV flatfields for the four bluest filters (in blue). After reprocessing with the improved flatfields, the previously large scatter in the UV for early observations is brought down to a level similar to that of the longer wavelength filters.

The subset of data excluding the early observations no longer warrants separate treatment as it did in the previous report because the UV scatter is not significantly greater. Figure 5 shows analogous plots of Δ Flux vs. Time for GRW70 through F225W. The plot on the left shows data processed with the old UV flats, and the figure on the right shows data processed with the improved UV flats. The large degree of scatter in the earliest observations is removed when images are reprocessed with the 2016 flatfields. Some of the remaining scatter can be attributed to lower signal-to-noise in earlier observations due to shorter exposure times, which have since been increased.
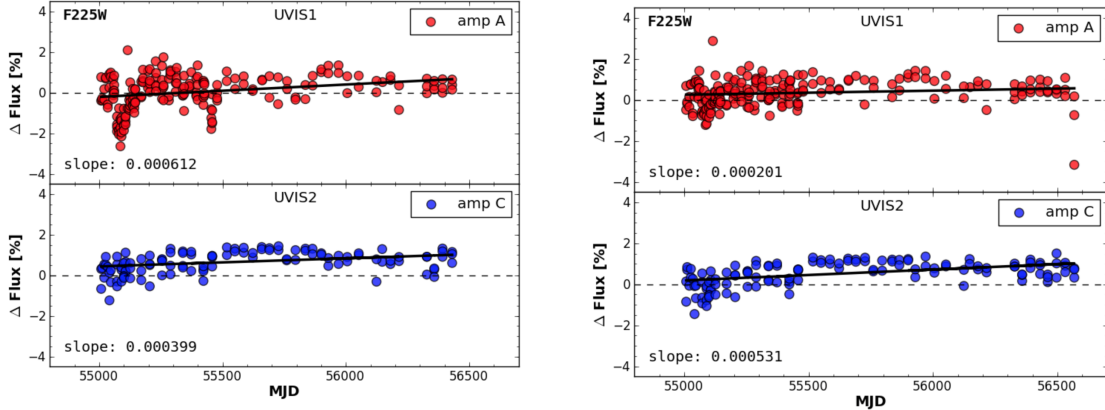
14

Fig. 5.— Throughput stability measured for images of GRW70 in F225W processed in 2014 (left) and reprocessed with the improved 2016 UV flats (right). The scatter in the earliest observations (MJD<55500) where the star's position was variable and moved across low and high sensitivity regions of the flatfield crosshatch pattern (Figure 4), is improved when reprocessing with the new UV flats.

4.2 Longterm Trends

With a few exceptions, we see in declines in measured countrates over time for both GRW70 and GD153 on both chips of the detector in most filters. Overall these declines are slightly greater on UVIS1 compared to UVIS2. These decreases in flux range from approximately 0.01 to 0.3 percent per year. The UV filters are comparatively more stable over time; we see only small declines or even slight increases in throughput on the blue end. Figure 6 and Figure 7 show the measured slopes plotted for each filter in order of increasing wavelength for GRW70 and GD153, respectively. Errors on the slopes are the standard deviations of the distribution of slopes fit to 10000 iterations of randomly selected subsets of the data.

GRW70 is relatively stable over time at UV wavelengths. Slopes of Δ Flux vs. time are close to flat, with some filters exhibiting small increases in throughput and some exhibiting small decreases. In the four bluest filters, we see a slight increase in countrate over time of GRW70 on UVIS2, roughly 0.02% per year for each filter. On UVIS1 only F225W shows a slight increase (0.024% per year) with the others showing small declines of 0.001 to 0.05 percent per year.

GD153 also exhibits nearly flat response over time in the UV except for filter F218W

15

where declines of 0.1126 and 0.2727 percent per year are measured on UVIS1 and UVIS2, respectively. As evident in Figure 7 and Table 5, the error on the linear fit to F218W data for GD153 on both chips was poor. F225W is nearly flat on UVIS1, while UVIS2 exhibits a stronger decline for this filter. Otherwise, like GRW70, we see only small positive or negative trends in throughput for GD153 in UV filters.

The intermediate wavelength F438W and redder control filters see the largest declines in throughput over time with the exception of F814W for both stars and F850LP for GRW70. In particular, F606W shows the sharpest declines for GRW70 on both chips (-0.31% per year on UVIS1, -0.25% per year on UVIS2), and for GD153 on UVIS1 (-0.33% per year).
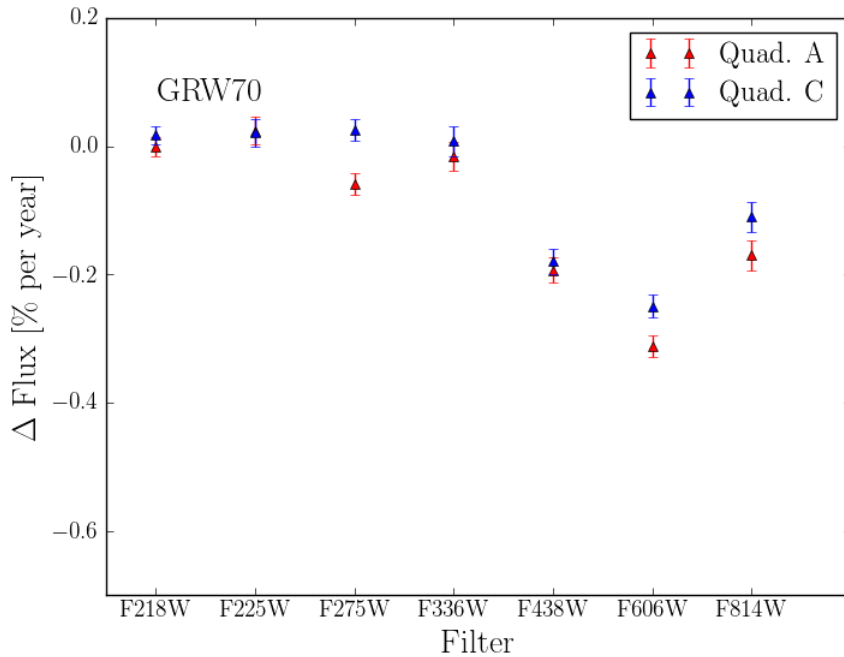

Fig. 6.— Flux losses as a function of wavelength based on linear fits to GRW70 in a subset of crucial blue filters (F218W, F225W, F275W, F336W, 438W) and control filters (F606W and F814W). Error bars are standard deviation from the Monte Carlo simulations.
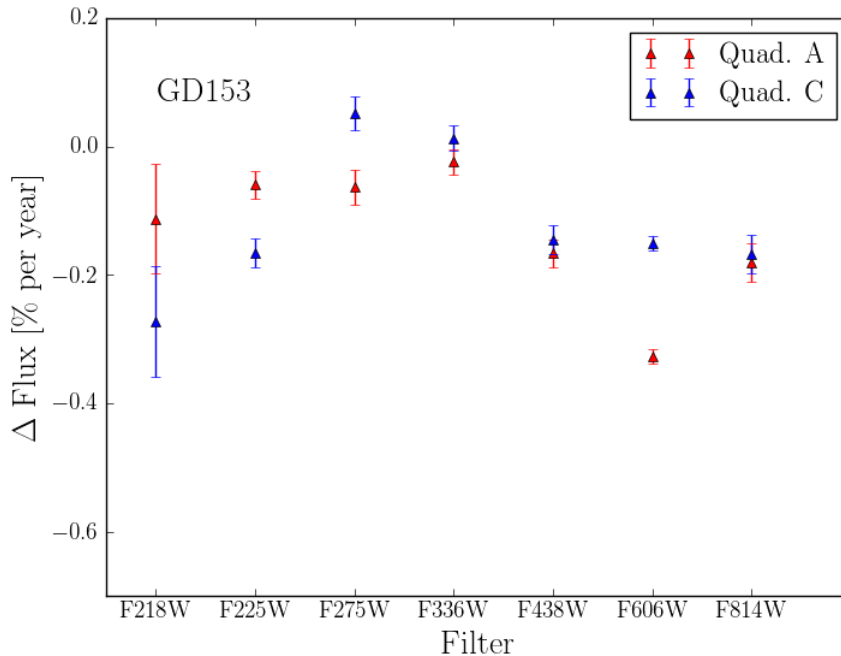
Fig. 7.— Flux losses as a function of wavelength based on linear fits to GD153 in a subset of crucial blue filters (F218W, F225W, F275W, F336W, 438W) and control filters (F606W and F814W). Error bars are standard deviation from the Monte Carlo simulations.

The cause for these observed downward trends in WFC3/UVIS remains unclear. Several possible explanations, including CTE, breathing, drifts in the absolute and relative gain, readnoise, filter degradation, sky correction methods and instrument stability have all been ruled out (G14, section 4.2).

4.3 Contamination

Contaminants on the CCD windows would manifest as a decline in throughput. All known contaminants are particularly opaque to UV wavelengths, therefore we would expect to see throughput decline in the UV faster than in longer wavelength filters. The Wide Field Planetary Camera 2 (WFPC2) on HST, for example, suffered from contamination due to the cold CCD window. WFPC2 demonstrated declines in throughput that were steeper in the UV (Gonzaga et al., 2010, section 5.2). A routine decontamination program that warmed the windows every month successfully removed short-term contaminants.

Frequent observations of GRW70 and GD153 in UV filters, and redder control filters, provide a long-term data set to analyze the throughput stability of the detector. We effectively see the opposite of the signature for contamination: declines in throughput are greater in redder filters than in the UV. At this time, we conclude that there are no obvious contaminants on the CCD windows.

5. Conclusion

By analyzing data spanning from SMOV to the present (2009-2017), we see slight declines in throughput in most filters on both CCD chips, ranging from about 0.01 to 0.3 percent per year. These declines are greater in longer wavelength filters. We speculate that there may be an underlying slow, uniform decline in throughput across all wavelengths that is offset in bluest filters, resulting in slower declines in the UV than in the red. The mechanism for this decline is not yet understood, although several likely culprits, such as drifts in the absolute and relative gain, filter degradation and instrument stability, have been ruled out.

5. Future Work

We will continue to make routine observations of GRW70 and GD153 and measure the change in countrate over time, prioritizing observations of GD153 to build up a comparable data set to the long history of GRW70 observations.

In an attempt to achieve higher signal-to-noise, we are investigating the photometric repeatability of spatially scanned standard stars in place of the current staring mode program with HST program 14878. This is motivated by the potential photometric repeatability of 0.1% seen in high precision photometry using spatial scans (HST Program 14020, P.I McCullough). If the results from 14878 are found to be repeatable, we may consider transitioning the contamination and stability monitor from staring to scanning mode.

6. Acknowledgments

Proposal ID	Subarrays	Filters	Exposure Time (sec)	Post-Flash?
11426	UVIS1-C512A-SUB, UVIS2-C512C-SUB	F225W, F275W, F300X, F343N, F218W, F336W, F395N, F410M, F280N, F390M, F373N, F390W, F467M, F438W, F606W, F814W	1.4,1.3,0.48,1.6,3.9,0.8, 5.3,2.0,23.8,2.1,10.2, 0.48, 1.8,0.48,0.48,1.0	No
11907	UVIS1-C512A-SUB, UVIS2-C512C-SUB, UVIS2-C512B-SUB, UVIS2-C512D-SUB	F275W, F336W, F225W, F390M, F547M, F438W, F390W, F475W, F606W, F814W, F218W	2.0,1.5,2.0,4.0,1.5,1.0, 1.0,1.0,0.48,2.0,6.0	No
12333	UVIS1-C512A-SUB, UVIS2-C512C-SUB	F218W, F275W, F336W, F390M, F390W, F438W, F547M, F555W, F606W, F467M, F225W, F475W, F814W, F850LP, F300X, F469N, F502N	17.6,6.0,4.0,11.0,2.1, 3.1,4.0,1.5,1.3,8.6,6.3, 1.5,6.2,32.5,1.0,48.0, 33.4	No
12698	UVIS1-C512A-SUB, UVIS2-C512C-SUB	F225W, F336W, F275W, F555W, F606W, F300X, F438W, F814W, F218W, F475W, F547M, F467M, F390M, F850LP, F390W, F502N	6.3,4.0,6.0,1.5,1.3,1.0, 3.1,6.2,17.6,1.5,4.0, 8.6, 11.0,32.5,2.1,33.4	No
13088	UVIS1-C512A-SUB, UVIS2-C512C-SUB	F218W, F225W, F275W, F336W, F438W, F606W, F814W, F300X	17.6,6.3,6.0,4.0,3.1, 1.3,6.2,1.0	Yes
13574	UVIS1-C512A-SUB, UVIS2-C512C-SUB	F218W, F225W, F275W, F225W, F225W, F336W, F438W, F606W, F814W, F300X, F438W, F438W, F438W, F336W, F336W	17.6,6.3,6.0,2.0,4.0, 4.0,3.1,1.3,6.2,1.0, 0.48,1.0, 2.0,0.8,1.6	Yes
14018	UVIS1-C512A-SUB, UVIS2-C512C-SUB	F218W, F225W, F275W, F336W, F438W, F606W, F814W, F300X, F300X, F390M, F547M, F390W, F410M, F467M, F475W, F555W, F850LP	17.6,6.3,6.0,4.0,3.1,1.3, 6.2,1.0,3.7,12.5,5.0,2.4, 11.0,10.0,2.0,1.6,36.0	Yes
14382	UVIS1-C512A-SUB, UVIS2-C512C-SUB	F606W, F814W, F336W, F218W, F225W, F275W, F438W, F300X	1.3,6.2,4.0,17.6,6.3, 6.0,3.1,1.0	Yes
14815	UVIS1-C512A-SUB, UVIS2-C512C-SUB	F606W, F814W, F336W, F218W, F225W, F275W, F438W, F300X	1.3,6.2,4.0,17.6,6.3, 6.0,3.1,1.0	Yes

Table 2: Calibration monitoring programs for GRW70 from SMOV through Cycle 24. For each proposal ID, this table includes the subarrays where images were taken, the filters used and by index the corresponding exposure times, and the post-flash status.

Proposal ID	Subarrays	Filters	Exposure Time (sec)	Post - Flash?
12334	UVIS2-M512C-SUB	F225W,F275W,F336W, F390W,F438W,F555W, F606W,F814W,F850LP	6.5,7.0,5.5,3.3,6.0, 3.1,2.2,15.0,25.0	No
12699	UVIS2-M512C-SUB	F438W,F606W,F336W, F814W,F225W,F275W, F390W,F850LP,F555W	6.0,2.2,5.5,15.0, 6.5,7.0,3.3,25.0, 3.1	No
13089	UVIS1-C512A-SUB, UVIS1-C512D-SUB	F218W,F225W,F336W, F275W,F300X,F390W, F438W,F850LP,F814W, F606W,F555W,F390M, F343N,F547M,F373N, F395N,F469N,F502N, F467M,F410M,F280N, F395N	12.4,5.0,4.5,5.4,1.0, 3.0,5.5,18.0,11.5, 3.0,3.0,14.5,9.4,8.0, 10.5,35.5,15.0,11.0, 17.0,16.0,17.0,35.0	Yes
13575	UVIS2-M512B-SUB, UVIS2-M512C-SUB	F300X,F850LP,F218W, F225W,F275W,F336W, F390W,F438W,F555W, F606W,F390M,F410M, F467M,F814W,F343N, F547M,F373N,F395N ,F502N,F280N,F469N, F850LP,F395N	1.0,23.0,12.4,5.0, 5.4,4.5,3.0,5.5,3.0, 3.0,14.5,16.0,17.0, 11.5,9.4,8.0,10.5, 35.5,11.0,17.0,15.0, 18.0,35.0	Yes
14021	UVIS1-C512A-SUB, UVIS2-C512C-SUB	F218W,F225W,F275W, F336W,F438W,F555W, F606W,F814W,F547M	12.4,5.0,5.4,4.5,5. 5,3.0,3.0,11.5,8.0	Yes
14382	UVIS1-C512A-SUB, UVIS2-C512C-SUB	F814W,F275W,F336W, F218W,F225W,F438W, F606W,F300X	11.5,5.4,4.5,12.4, 5.0,5.5,3.0,1.0	Yes
14384	UVIS1-C512B-SUB, UVIS2-C512D-SUB	F438W,F555W,F218W, F606W,F814W,F225W, F547M,F275W,F336W	5.5,3.0,12.4,3.0, 11.5,5.0,8.0,5.4,4.5	
14815	UVIS1-C512B-SUB, UVIS2-C512D-SUB	F438W,F555W,F218W, F606W,F814W,F225W, F547M,F275W,F336W	5.5,3.0,12.4,3.0, 11.5,5.0,8.0,5.4,4.5	

Table 3: Calibration monitoring programs for GD153 from Cycle 18 through Cycle 24. For each proposal ID, this table includes the subarrays where images were taken, the filters used and by index the corresponding exposure times,and the post-flash status.
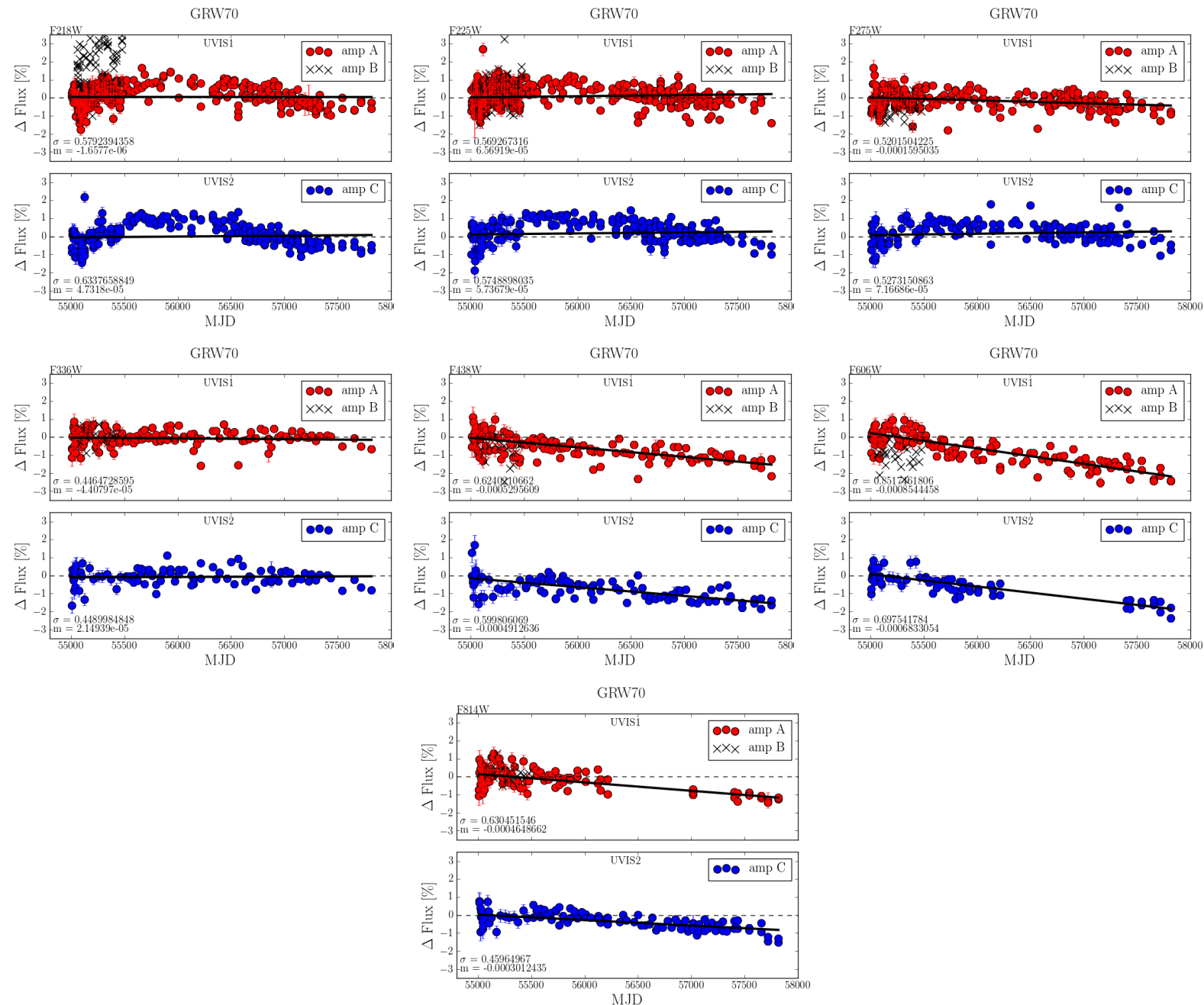
Fig. 8.— All observations of GRW70 in the subset of key UV and blue filters (F218W, F225W, F275W, F336W, 438W) and longer wavelength control filters (F606W and F814W) that have been observed continuously from SMOV (July - August 2009) to the present. The Y axis is the percent difference in count rate, Δ Flux [%]. This was calculated by finding the median value of flux for all the observations in the first visit and taking the percent difference from that average flux for each subsequent measurement. The x axis is the Modified Julian Date (MJD). Observations marked with 'X' are data taken in amplifier quadrants B and D, and these values are not included in the linear fit due to the limited date range. The slope is fitted to all observations from quadrants A and C, respectively, and weighted by the propagated errors on the individual observations. Slopes (m) are listed on each plot, in units of Δ Flux [%] / Day. Standard deviations σ (scatter in the data) are also given for each filter / quadrant. See table 4 for statistics for these full data sets.
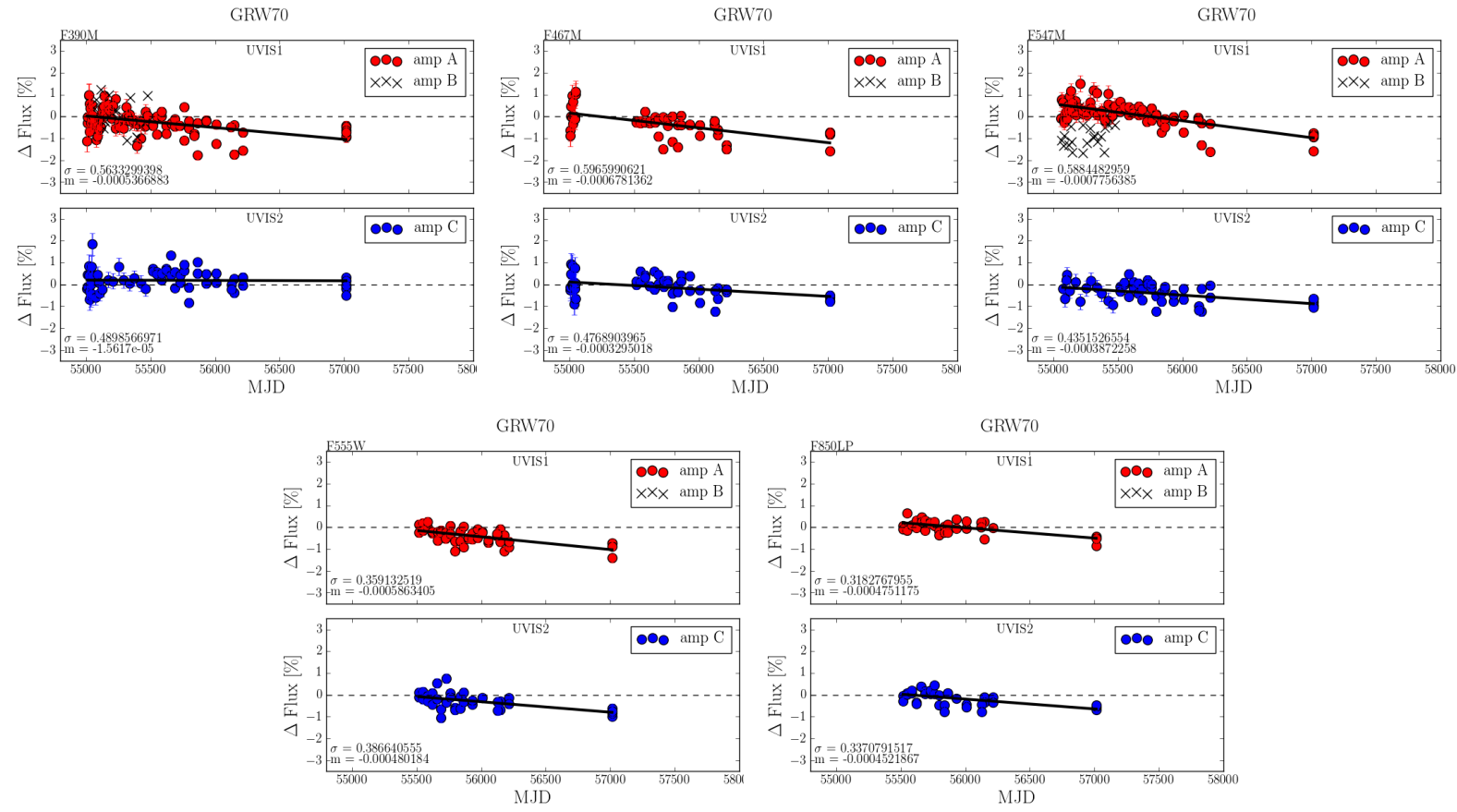
Fig. 9.— All observations of GRW70 in the subset of less commonly used filters that have been observed continuously from SMOV (July-August 2009) to the present). See Figure 8 for more information.
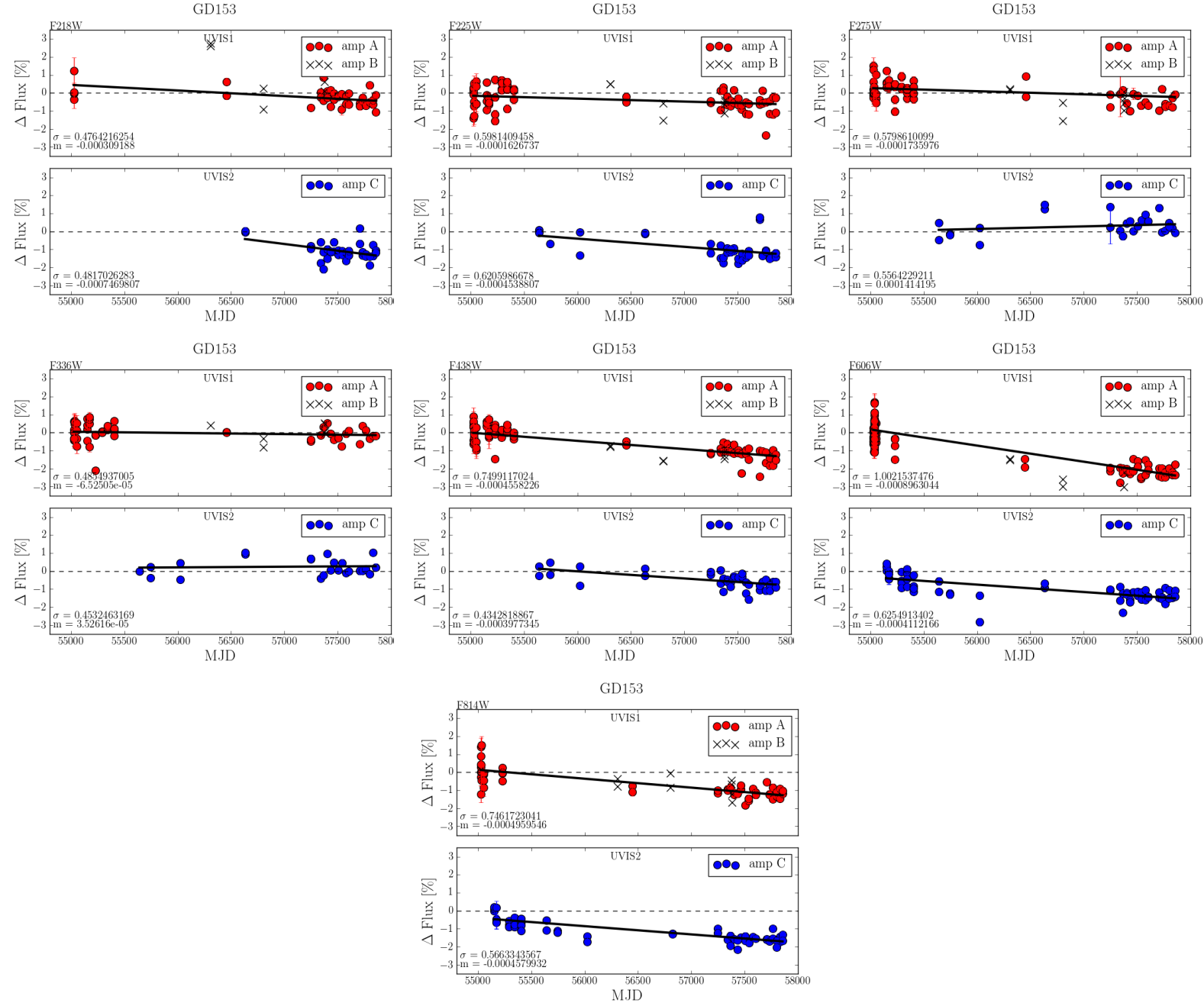
Fig. 10.— All observations of GD153 in the subset of key UV and blue filters (F218W, F225W, F275W, F336W, 438W) and longer wavelength control filters (F606W and F814W) that have been observed continuously from SMOV (July - August 2009) to the present. See Figure 8 for more details and Table 5 for statistics for these datasets.

	Amp A			Amp C		
Filter	Slope	Mean	Stdev.	Slope	Mean	Stdev.
F218W	-0.0006	0.0006	0.0140	0.0173	-0.0035	0.0196
F225W	0.0240	0.0026	0.0215	0.0210	0.0060	0.0196
F275W	-0.0582	-0.0596	0.0165	0.0262	0.0110	0.0230
F336W	-0.0161	-0.0068	0.0228	0.0078	0.0063	0.0265
F390M	-0.1959	-0.1961	0.0488	-0.0057	0.0022	0.0480
F438W	-0.1933	-0.1818	0.0196	-0.1793	-0.1720	0.0315
F467M	-0.2475	-0.2611	0.0613	-0.1202	-0.1221	0.0499
F547M	-0.2831	-0.2771	0.0384	-0.1413	-0.1502	0.0378
F555W	-0.2140	-0.2281	0.0573	-0.1753	-0.1808	0.0429
F606W	-0.3119	-0.3114	0.0176	-0.2494	-0.2472	0.0212
F814W	-0.1697	-0.1712	0.0231	-0.1100	-0.1121	0.0221
F850LP	-0.1734	-0.2660	0.1238	-0.1650	-0.1860	0.0455

Table 4: Long term trends for GRW70. For each amplifier quadrant, the 'Slope' column is the slope of the linear fit to the data over the full date range. The 'Mean' and 'Stdev.' columns are the mean and standard deviation of the distribution of random slopes from the Monte Carlo simulations, respectively.

	Amp A			Amp C		
Filter	Slope	Mean	Stdev.	Slope	Mean	Stdev.
F218W	-0.1129	-0.1188	0.0865	-0.2726	-0.2334	0.1590
F225W	-0.0594	-0.0597	0.0219	-0.1657	-0.1653	0.0614
F275W	-0.0634	-0.0836	0.0268	0.0516	0.0624	0.0563
F336W	-0.0238	-0.0273	0.0195	0.0129	0.0095	0.0604
F438W	-0.1664	-0.1801	0.0224	-0.1452	-0.1448	0.0391
F606W	-0.3272	-0.3260	0.0113	-0.1501	-0.1502	0.0171
F814W	-0.1810	-0.1860	0.0300	-0.1672	-0.1665	0.0196

Table 5: Long term trends for GD153. For each amplifier quadrant, the 'Slope' column is the slope of the linear fit to the data over the full date range. The 'Mean' and 'Stdev.' columns are the mean and standard deviation of the distribution of random slopes from the Monte Carlo simulations, respectively.

REFERENCES

Bajaj, V., Khandrika, H., 2017, WFC3 ISR 2017-10: "Comparing Aperture Photometry Software Packages".

Bohlin, R., 1996, "Spectrophotometric Standards from the Far-UV to the Near-IR on the White Dwarf Flux Scale".

Bohlin, R. Landolt, A., 2015, "The CALSPEC Stars P177D and P330E".

DeMarchi, G et al., 2004, ACS ISR 2004-08: "Detector Quantum Efficiency and Photometric Zero Points of the ACS".

Deustua, S et al., 2016, WFC3 ISR 2016-03: "UVIS 2.0 Chip-dependent Inverse Sensitivity Values".

Gosmeyer, C. M., 2014, WFC3 ISR 2014-20: "Update on the WFC3/UVIS Stability and Contamination Monitor".

Gonzaga, S., Biretta, J. et al., 2010, HST WFPC2 Data Handbook, v. 5.0, ed.

Kalirai, J et al., 2010, WFC3 ISR 2010-14: "The Photometric Performance of WFC3/UVIS: Temporal Stability Through Year 1".

Mack, J et al., 2013, WFC3 ISR 2013-10: "In-flight Corrections to the WFC3 UVIS Flat Fields".

Mack, J., 2016, WFC3 ISR 2016-05: "UVIS 2.0: Ultraviolet Flats ".

Mack, J et al., 2016, WFC3 ISR 2016-04: "UVIS 2.0: Chip-Dependent Flats".

Noeske, K et al., 2012, WFC3 ISR 2012-09: "WFC3 UVIS Charge Transfer Efficiency October 2009 to October 2011".

Ryan, R et al., 2016, WFC3 ISR 2016-01: "The Updated Calibration Pipeline for WFC3/UVIS: A Reference Guide to Calwf3 3.3".

Sirianni M et al., 2005, PASP, 117, 1049.

Stys, D., Walborn, N., 2001, STIS ISR 2001-01: "Sensitivity monitor report for the STIS first-order modes-III".

Whitmore, B., Heyer, I., Baggett, S., 1996, WFPC2 ISR 1996-04: "Effects of contamination on WFPC2 photometry".

van Dokkum, P. G., 2001, PASP, 113, 1420.